N-Polar III- Nitride Optoelectronic Devices

Thesis

Presented in the Partial Fulfillment of the Requirements for the Degree Master of Science in the Graduate School of the Ohio State University

By

Fatih Akyol

Graduate Program in Electrical and Computer Science

The Ohio State University

2011

Master's Examination Committee:

Professor Siddharth Rajan, Advisor

Professor Roberto C. Myers

Abstract

III-Nitride semiconductors have a tunable direct band gap starting from 0.7 to 6.2 eV, which makes them one of the most useful material systems especially for optoelectronic applications.

Regarding to the solar cell applications, the highest efficiencies have been reported by using InGaP/(In)GaAs/Ge multi-junction solar cells. Since this material system is limited with a widest applicable band gap for InGaP around 1.86 eV, highest solar cell efficiencies has been limited by lack of solar cells having a band gap around 2.3 eV. In this research, 2.3 eV InGaN p-i-n solar cells has been simulated and shown that the optimum thickness of the intrinsic layer thickness is a strong function of minority carrier mobility and lifetime. The results indicated that efficiency of InGaN p-n junction solar cells can be enhanced ~35% by using optimized p-i-n designs.

III-Nitrides have been widely used for light emitting diode (LED) applications. The researches have been conducted on devices grown various crystal planes including c-(Ga-polar), semi-polar and non-polar planes. However, based on our knowledge, the N-polar orientation of c-plane has not been studied both theoretically and experimentally. Thus, in this report, the Silvaco Atlas simulations have been carried out for both Ga-polar and N-polar single quantum well blue LEDs. The results have pointed out that N-polar LEDs show much less electron and hole overflow current with ~ 1V less turn-on voltage operation compared to Ga-polar LEDs. In the experimental part, the first N-polar green

led grown by molecular beam epitaxy (MBE) has been demonstrated. The device showed peak emission wavelengths varying from 564.5 to 540 nm. The full width at half-maximum reduced from 74 to 63 nm as the drive current was increased to 180 A/cm^2.

Dedication

Dedicated to my family

Acknowledgements

I would like to thank to my advisor Prof. Siddharth Rajan for his ideas and advices. I've learned fundamentals of theatrical and experimental work from his precious suggestions. Also, I'm thankful to all of our research group members (Siriram Krishnamoorty, Michele Espesto and others) especially Digbijoy Nath who has grown the N-polar LEDs and Pil Sung Park who has developed the process for fabrication and helped me for using Silvaco Atlas simulation. I thank Prof. Roberto Myers for being my exam committee member. Lastly, I want to specially thank to Dr. Mutlu Kundakci and Dr. Emre Gur for their support and sincere suggestions.

Vita

February 1985…….Born in Corum, Turkey

2008…….B.S. Electrical and Electronic Engineering, Gaziantep University

Publications

[1] Fatih Akyol, Digbijoy N. Nath, Emre Gur, Pil Sung Park and Siddharth Rajan: Jpn. J. Appl. Phys. **50** (2011) 052101.

Fields of Study

Major Field: Electrical and Computer Engineering

Table of Contents

List of Tables

List of Figures

Chapter 1: Introduction to III-Nitride Optoelectronic Devices

1.1 History of GaN Light Emitting Diodes

Single crystal GaN was grown for the first time by Maruska and Tietjen using hydride vapor phase epitaxy in 1969. Intrinsic properties such as the direct band gap of 3.39 eV and the n-type conduction in the undoped crystal were determined. Since p-type doping of GaN couldn't be realized, the researches on light emitting diode (LED) operation was relatively poor. There were only few reports of light emission from GaN crystal. The first LED was fabricated by Pankove and co-workers using an undoped n-type GaN crystal and an insulating Zn-doped layer and an indium metal contact forming a metal-insulator-semiconductor type LED with an emission in green region in 1971 [1]. The following year, Maruska reported violet emission (430 nm) from a Mg-doped GaN crystal via tunneling of electrons through a triangular-potential-well which is not an efficient way of LED operation [2,3]. The first molecular beam epitaxy (MBE) growth of single crystal GaN was achieved by Akasaki *et al* in 1974 [4]. It was demonstrated in 1985 that growth of optically flat and free of cracks GaN crystal can be grown on sapphire substrate by metalorganic vapor phase epitaxy (MOCVD) after a nucleation layer of AlN layer was introduced during the growth [5]. However, AlN buffer layer was not appropriate for InGaN growth due to the large lattice mismatch between AlN and InN. The next breakthrough of nitride growth came in 1992 when low defect density InGaN crystal grown on low-temperature growth of GaN crystal on sapphire substrate [6].

For efficient emitters the p-type conductivity is crucial. The first p-type conductivity was realized by Akasaki and his co-workers using low energy electron-beam irradiation in 1989 [7]. After two years, more practical way of Mg-activation was realized by Nakamura *et al* using high temperature thermal annealing in nitrogen ambient [8].

The first nitride p-n junction LED with emissions in UV and violet-blue region was fabricated by Akasaki *et al.* in 1989 [7]. Nakamura *et al.* demonstrated the first blue and green LEDs in 1993 and 1995 respectively [9, 10]. After those establishments on c-plane (Ga-polar) orientation, nitride LEDs has grown rapidly. Today, nitride LEDs can be successfully grown also on non- and semi-polar planes with high efficiencies.

1.2 Fundamentals of III-Nitrides

1.2.1 Polarization in III-Nitride Crystals

III-Nitride crystals can be grown as wurtzite or zincblende crystal structures. Since wurtzite nitrides are thermodynamically more stable, they are preferred for device applications especially for optoelectronic devices. Figure 1.1 (a) and (b) shows the GaN crystal structures of zincblende and wurtzite respectively. The direction of the dipole moment points from nitrogen (yellow sites) to gallium (grey sites) atoms. In a GaN zincblende structure total dipole moment is zero for each individual atom whereas; it is non-zero for a wurtzite crystal which results from the lack of inversion symmetry. The resulting polarization along [0001] direction is called spontaneous polarization (SP). The axis along this direction is called as c-plane which can end up with Ga or N atoms depending on the growth direction. Figure 1.2 (a) and (b) depicts Ga- and N-face crystals

together with the direction of SP for each one respectively. SP is in the opposite direction of the growth for Ga-polar crystals while it is along the growth direction for an N-polar crystal. Both crystals have been investigated with theoretical and experimental studies [11, 12, 13].

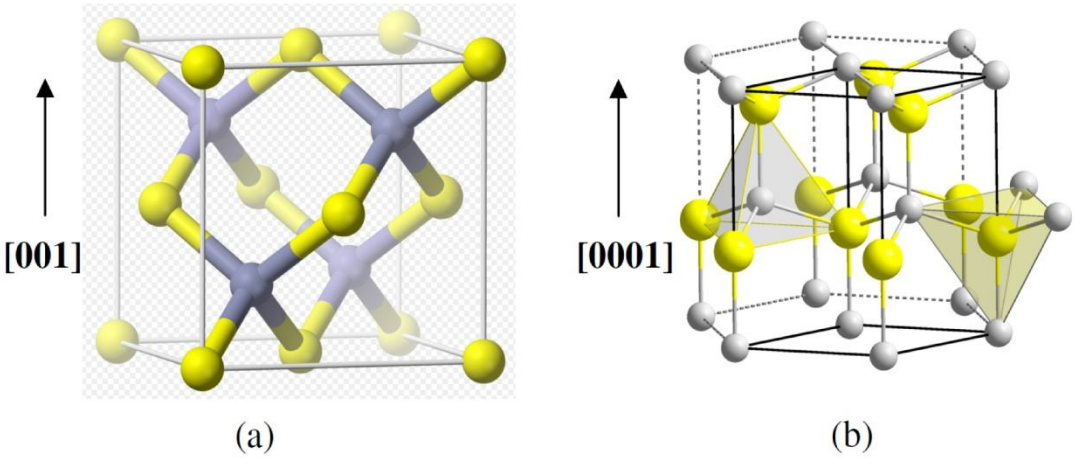

Figure 1.1 GaN crystals in (a) zincbelnde and (b) wurtzite structure.

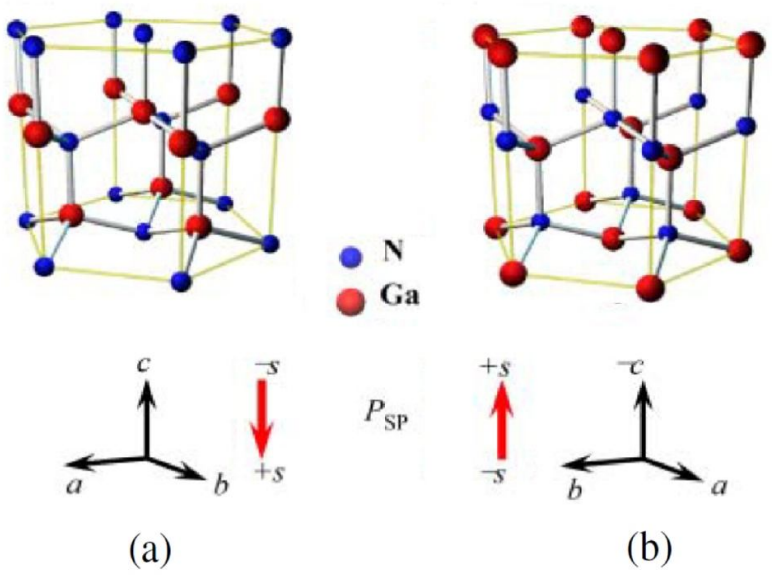

Figure 1.2 (a)Ga-polar and (b)N-polar wurtzite GaN crystals and the directions of spontaneous polarization.

Table 1.1 shows the lattice parameters and polarization constants of III-nitrides [14,15]. The piezoelectric polarization (PZ) induces due to strain in the epitaxial layers. The value of PZ along [0001] axis p_{pe} is calculated using the following relation.

$$p_{pe} = e_{33}\frac{c-c_0}{c_0} + e_{31}\frac{a-a_0}{a_0}, \qquad 1.1$$

where a_0 and c_0 is the lattice parameters of the strained layers, e_{33} and e_{31} are PZ polarization constants given in Table 1.1. Using the Eqn. 1.1, it can be figured out that a compressive strain to a lattice results in a PZ in the opposite direction of SP whereas; a tensile strain induces PZ in the direction of SP in wurtzite crystals. Since lattice mismatch

between InN and GaN is quite high, PZ is dominant in In rich InGaN crystals. Conversely, SP is dominant in Al rich AlGaN samples. The polarization charges induce electric field in the crystal without any external effects such as built-in bias or light illumination. Total internal field under net polarization p is given by

$$E = -\frac{p}{\epsilon_r(x)\epsilon_0}, \qquad 1.2$$

where $\epsilon_r\ (x)$ represents the relative dielectric constant of the alloys. It has been reported that polarization induced electric fields can be as high as 15 MV/cm [16].

		GaN	**InN**	**AlN**
Lattice Constants	a (A)	3.189	3.534	3.111
	c (A)	5.185	5.718	4.978
Polarization parameters	p_{sp}(C/m2)	-0.029	-0.032	-0.081
	e_{31}(C/m2)	-0.49	-0.57	-0.6
	e_{33}(C/m2)	0.73	0.97	1.46

Table 1.1 Lattice constants and polarization parameters of GaN, InN and AlN.

1.2.2 Electronic Band Properties

All of the III-Nitride compounds are direct band gap semiconductors and can show exceptional optoelectronic properties. In direct band gap semiconductors radiative transition from conduction to valance band has much higher probability than in the case

of indirect band gap semiconductors such as silicon. Figure 1.3 depicts band gap versus lattice constant values for various semiconductor materials. It can be seen that III-nitrides alloys can be tuned in a wide energy range from ~0.7 to 6.2 eV covering the spectrum from infra-red to deep UV which takes further attention for III-nitrides optoelectronic applications such as LEDs and solar cells.

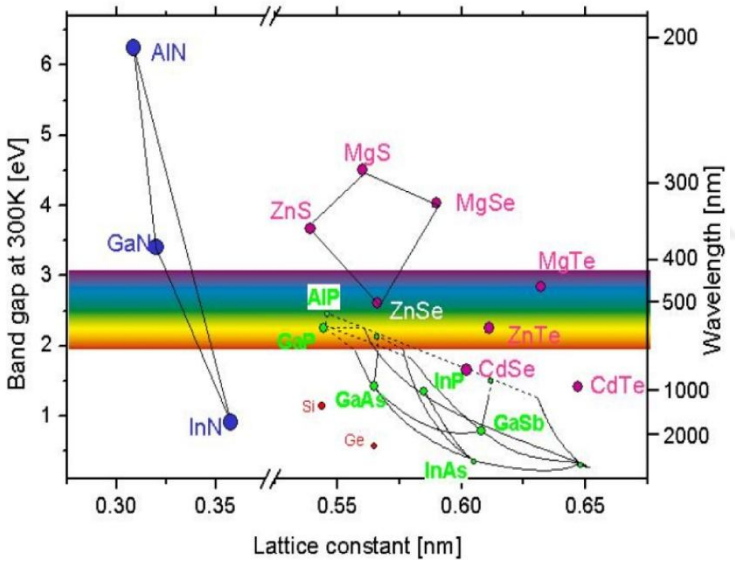

Figure 1.3 Band gaps and lattice constants of various material systems.

The presence of high spontaneous and piezoelectric polarization can affect the band diagrams of polar quantum-well (QW) structures dramatically. A sample band diagram of InGaN/GaN QW is shown in Figure 1.4 without (a) and with (b) polarization charges

[17]. It is seen in Fig 1.4(a) that electron and hole wave functions are in perfect match in a rectangular well whereas; it is in triangular shape for Figure 1.4(b). There are several effects of a triangular-well especially on LED operations. First of all, electrons and holes spatially separated in the QW which decreases the wave-function overlap and the spontaneous emission rate. Secondly, it is observed under low current regime that the emission energy reduces under strong polarization fields which is depicted in Figure 1.4(b) as a difference between discrete energy levels (E_1>E_2) so called quantum confined Stark effect (QCSE). Additionally, the wave-function penetration in to barrier regions is observed which decreases the confinement and can result in light emissions in barrier regions [18]. To reduce and eliminate such problems caused by polarization field, crystal growths along semi- and non-polar planes has been widely investigated.

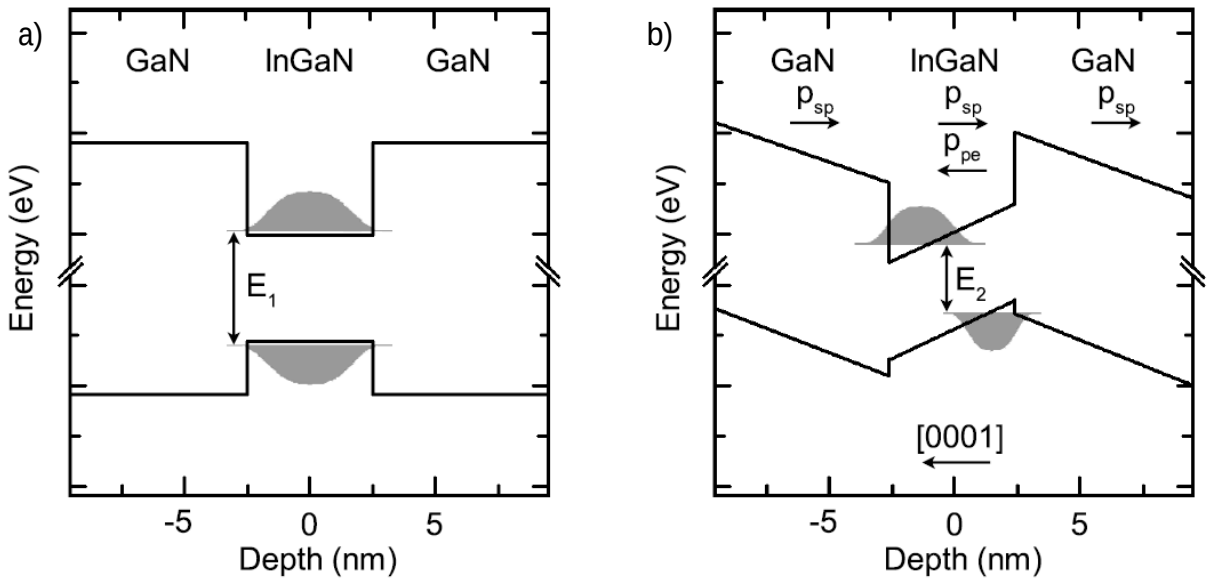

Figure 1.4 A sample band diagram of InGaN/GaN QW (a) without and (b)with polarization charges

1.3 Solar Energy and High Efficiency Efforts

It is reported that 97.1% of world energy production is from fossil fuels and nuclear power [19]. Oil, coal, natural gas and biomass are the major fossil energy sources from which high amount of CO_2 releases. CO_2 is a greenhouse gas and considered to be the reason of the global warming. On the other hand, nuclear power is not harmful for the atmosphere. But, the remnants of nuclear reaction remain radioactive for many years and should be stored in particular chambers during this time. Since world's energy consumption increases rapidly, suffering from side effects of our major energy sources is expected to increase unless renewable energy sources dominates the area. It is reported that the potential of solar irradiation is at least 1000 times greater than that of the summation of all other renewable energy sources which makes direct solar irradiation to be the only global renewable energy source [20].

Photovoltaic (PV) is the direct energy conversion from light to electrical energy. The process can be explained in such a way that incoming photons present in light waves penetrate into a solar cell and if they are absorbed, electron-hole pairs can be created. Depending on the cell designs, the carriers can be separated and move in single direction toward the corresponding terminals. This additional light generated current in the material can supply direct current (dc) electricity to the load. There are different structures used for solar cell fabrications such as bulk materials, thin films, organic polymers and organic dyes. Although, majority of the commercially available solar cells are made from relatively low-cost Silicon (Si) bulk crystal, even lower cost thin film, organic-inorganic PV systems have been investigated to compete with fossil fuels and

nuclear energy. On the other hand, the researches towards high efficiency multi-junction solar cells are also focus of interest in concentrated PVs and extraterrestrial applications.

The efficiency enhancement of various solar cells up to date is given in Figure 1.5 [21]. It can be seen that almost all of the solar cell studies has become mature with an exception of organic solar cell studies which are towards the realization of low cost solar cells. To date, the top most PV efficiency of 42.3% has been realized by three-junction InGaP/(In)GaAs/Ge based devices under a solar concentration of 406 suns. Higher

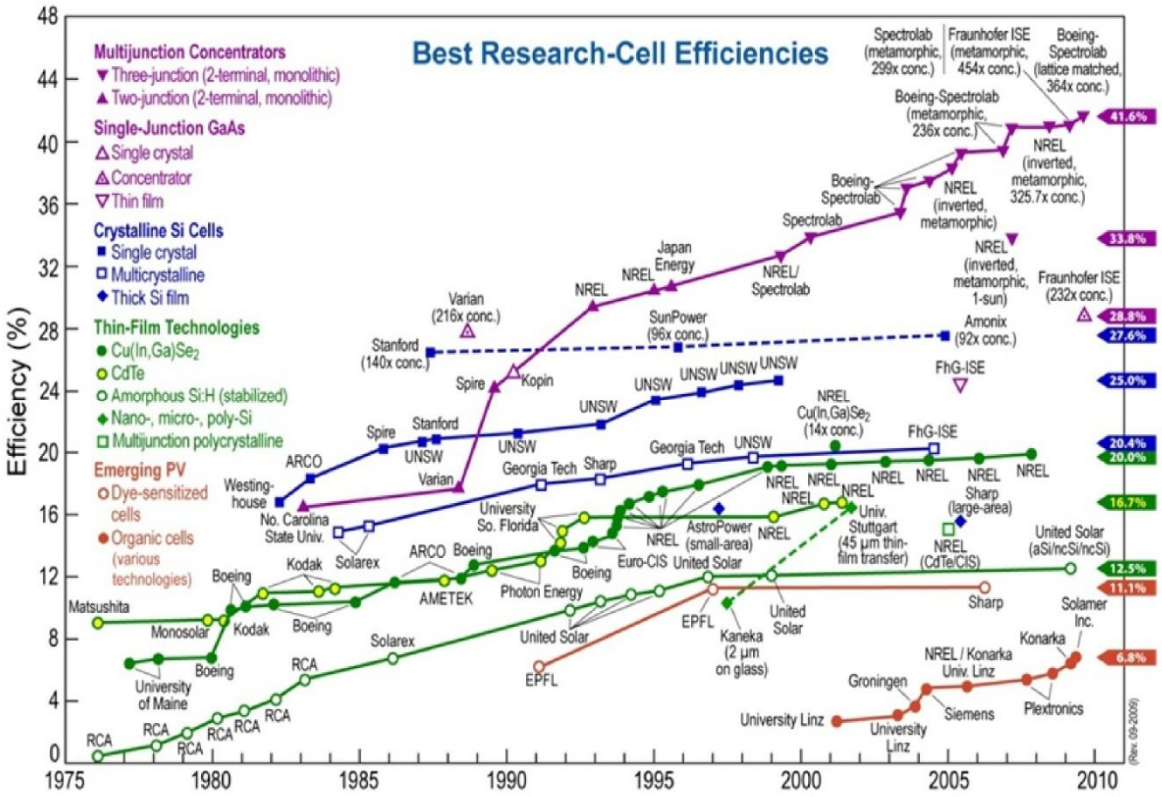

Figure 1.5 Historical developments of best solar cell efficiencies from various materials [21].

efficiencies can be realized by using multiple band gaps for solar cells. For a single junction solar cell, only the photon energies higher than the band gap of the material is absorbed with an heat conversion of the excess energy of the photons above the band gap energy and the rest of the photons with energy lower than the band gap can't be absorbed by the material. In the case of a multi-junction solar cell, introduction of additional active regions with higher band gap materials to the top and lower ones to the bottom as indicated in Figure 1.6. Higher energy photons are absorbed in high band gap window junction and lower energy photos are transmitted to the next junction and this process is

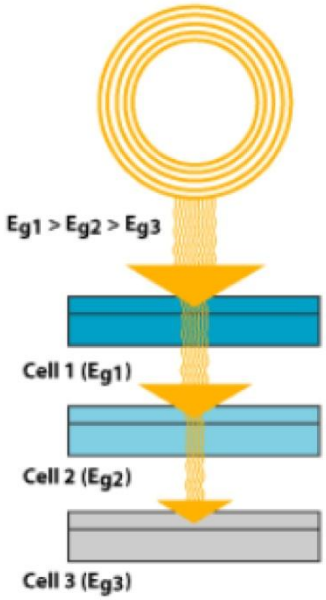

Figure 1.6 Light transfer through a three-junction solar cell

repeated for the following junctions which decreases energy converted to heat and the number of the photons transmitted without absorbed by a cell. Currently, the band gap of the InGaP window junction is ~1.8 eV however getting higher efficiency solar cells

requires using more than three junctions with the introduction of higher band gap (>1.8eV) semiconductors for the top cell.

The most promising material system to obtain higher efficiencies is InGaN (as discussed in section 1.2.2) whose band gap energy can be tuned from 0.7 eV to 3.4 eV. Such an energy variation can cover most of the solar spectrum. However, there are several drawbacks of InGaN alloys such as high lattice mismatch between InN and GaN, high polarization charges at GaN/InGaN interface and low carrier diffusion length [22]. First of all, due to the 11% lattice mismatch between InN and GaN, the growth of high In content InGaN layers results in relaxed layers with high structural defects which kills the minority carrier lifetime thus hinders light current generation. It is reported regarding to InGaP/(In)GaAs/Ge triple junction solar cells that even a lattice mismatch as low as 0.01% can significantly reduce the current generation[23]. Secondly, the presence of high piezoelectric polarization field across the active region of conventional Ga-polar solar cells has been simulated and shown to decrease the carrier collection dramatically [24]. The problems in those structures can be solved with the reversed polarization by growing the samples in N-polar orientation however there has been no N-polar InGaN solar cell demonstration till now [24]. Lastly, due to low carrier diffusion length in InGaN alloys (~200 nm), it is required to design pin structures to have drift assisted carrier collection. In the following chapter, the simulation of such a solar cell will be given to examine the characteristics of high In content InGaN homo-junction solar cells.

Chapter 2: The Simulation of ~2.3 eV InGaN Homojunction Pin Solar Cell

2.1. Introduction

By having a tunable band gap from ~0.7 to 3.4 eV, InGaN alloys can cover the whole visible spectrum and most part of the solar spectrum [25,26]. To date, it has been widely used in ultra-violet, blue and green light emitting and laser diodes [27,28,29]. Although it was successful for emitters, little research has been carried out for solar cell applications [30,31,32]. In addition to having a perfect match with the solar spectrum, InGaN alloys have been shown to have great properties for photovoltaic applications such as, high radiation damage resistant profile, direct band gap for entire alloy range and high absorption coefficient near the band edge [33,34].

Convensional solar cells have been designed with p-n junction configuration since, minority carrier diffusion length is high enough (for Silicon; few hundreds of microns) so that carrier collection probablity can be still high outside the depletion region whereas; GaN has been reported to have much shorter diffusion legths (~1μm) and InGaN has even lower diffusion lengths (~0.2 μm) which is a strong function of recombination centers in the material [35,36]. Because of the high latice mismatch between GaN and InN, material properties deteriodes for high Indium compositions which results in even shorter minority carrier diffusion lengths. Thus, it is required to

increase depletion region thickness for InGaN solar cells to collect more carriers. One way to do this is simply lightly doping of donor and acceptor to n and p sides respectively. However, this degrades open circuit voltage and minority carrier mobility of the solar cell. The other solution is the design of InGaN solar cells with p-i-n configuration which is realized by inserting an intrinsic region between p and n-regions. While keeping high doping concentrations at p and n regions, by varying the thickness of the intrinsic region depletion thickness can be controlled.

In this simulation, it is aimed to simulate a 2.3 eV InGaN homo-junction p-i-n solar cell by varying intrinsic layer thickness under standard AM0 solar spectrum. Since the actual minority carrier lifetime and mobility for InGaN is not well-known, the results will be addressed under a range of these parameters. It is expected that the results will foster the understanding of InGaN p-i-n solar cell operation towards the realization of high efficiency multi-junction solar cells.

2.2. Modelling and parameters

We used MATLAB to simulate the output characteristics of InGaN p-i-n solar cells. The designed InGaN p-i-n solar cell is shown in Figure 2.1. The thickness and doping concentration (N_A) of the p-type window layer was taken to be 70 nm and $5x10^{17}$ cm^{-3} respectively. N-type base layer was designed as 100nm thick with a doping concentration (N_D) of $5x10^{18}$ cm^{-3}. Intrinsic layer thickness was varied from 0 to 400nm.

For calculations, minority carrier hole mobility was assumed to be one-hundredth of the one for electrons. We used Modified Caughey Thomas theorem to find the electron mobility:

$$\mu_e = \mu_{min} + \frac{\mu_{max} - \mu_{min}}{1+(N_A/N_g)^{\gamma}}, \quad (1)$$

where μ_{max}, μ_{min}, N_g and γ are the particular parameters for semiconductors. For 30% InGaN the parameters are obtained using linear interpolation as 708.8 $cm^2V^{-1}s^{-1}$, 409.7 $cm^2V^{-1}s^{-1}$, 1x$10^7 cm^{-3}$ and 1.26 respectively [37, 38]. The equation was used unless calculations depend on electron mobility variation. $cm^2V^{-1}s^{-1}$

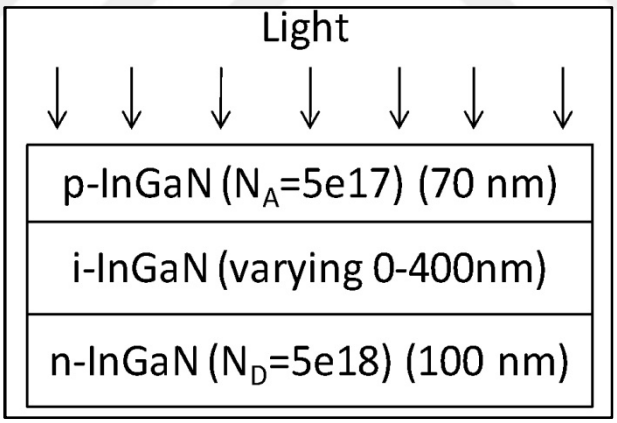

Figure 2.1. The structure of the simulated InGaN homojunction solar cell.

The constants for relative permittivity, effective density of states in conduction (N_C) and valance band (N_V) were determined by using linear interpolation, taking 30% InN composition in InGaN alloys which corresponds to the band gap value of 2.29eV (using

a bowing parameter of 1.43) [39,40]. By using these parameters the intrinsic carrier concentration was found as 0.593 cm^{-3} from the following equation:

$$n_i = (N_C . N_V)^{1/2} \, exp\left(-E_g/2k_B T\right), \tag{2}$$

The minority carrier diffusion length is given by:

$$L = \sqrt{D\tau}, \tag{3}$$

where τ is minority carrier lifetime which is assumed to be 50 ps except for the simulations using varied lifetime [41]. The diffusivity 'D' (cm^2/s) is calculated from Einstein relation :

$$D = (k_B T/\mathrm{q})\, \mu . \tag{4}$$

The front and back surface recombination velocity $S_{n,p}$ was assumed to be 4000 (cm/s) and reflection coefficient R is assumed to be 0.2 between air and InGaN interface. We used following equation to get wavelength dependent absorption coefficient $\alpha(\lambda)$ for 30% InGaN which is also shown in Figure 2.2. The parameters of the equation (5) was obtained by linear interpolation using the information given in reference [42]. It shows that the absorption coefficient of InGaN is taken to be higher than 10^5 cm^{-1} for the wavelengths shorter than 460nm.

$$\alpha(\lambda) = 10^5 \sqrt{2.6763\left(e(\lambda) - E_g\right) - 0.32197\left(e(\lambda) - E_g\right)^2}, \tag{5}$$

where $e(\lambda)$ is the wavelength dependent energy vector of the standard AM0 spectrum and E_g is the band gap energy (2.29 eV).

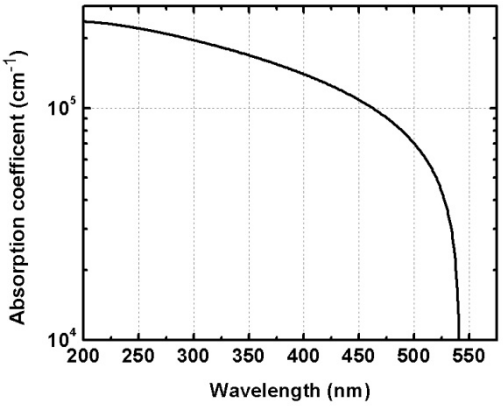

Figure 2.2. Absorption coefficient of 30% InGaN versus wavelength of the incoming light.

The electron (j_n) and hole (j_p) diffusion current densities were calculated using the following relations [43]:

$$j_n = \left(1 - \frac{W_{dep}{}^2}{\mu\tau(V_{bi}-V)}\right)\left(-\frac{q(1-R)b_s\alpha L_n}{(\alpha^2 L_n{}^2-1)}\right)*\left\{\frac{e^{-\alpha(x_p-w_p)}\left(\frac{S_nL_n}{D_n}cosh\frac{x_p-w_p}{L_n}+sinh\frac{x_p-w_p}{L_n}\right)-\left(\frac{S_nL_n}{D_n}+\alpha L_n\right)}{\frac{S_nL_n}{D_n}sinh\frac{x_p-w_p}{L_n}+cosh\frac{x_p-w_p}{L_n}}\right. +$$

$$\alpha Lne-\alpha xp-wp+q(Dnn0(eqVkbT-1)LnSnLnDncoshxp-wpLn+sinhxp-wpLnSnLn$$

$$Dnsinhxp-wpLn+coshxp-wpLn\,, \qquad (6)$$

and

$$j_p=\left(1-\frac{{W_{dep}}^2}{\mu\tau(V_{bi}-V)}\right)\left(-\frac{q(1-R)b_s\alpha {L_n}}{(\alpha^2{L_n}^2-1)}\right)\ e^{-\alpha(x_n-w_n)}$$

$$*\left\{\frac{\left(\frac{S_pL_p}{D_p}cosh\frac{x_n-w_n}{p}+sinh\frac{x_n-w_n}{L_p}\right)-\left(\frac{S_pL_p}{D_p}+\alpha L_p\right)e^{-\alpha(x_n-w_n)}}{\frac{S_pL_p}{D_p}sinh\frac{x_n-w_n}{L_p}+cosh\frac{x_n-w_n}{L_p}}-\ \alpha L_p\right\}+$$

$$\frac{q(D_pp_0(e^{\frac{qV}{k_bT}}-1)}{L_p}\left\{\frac{\frac{S_pL_p}{D_p}cosh\frac{x_n-w_n}{L_p}+sinh\frac{x_n-w_n}{L_p}}{\frac{S_pL_p}{D_p}sinh\frac{x_n-w_n}{L_p}+cosh\frac{x_n-w_n}{L_p}}\right\}, \tag{7}$$

where W_{dep} is total thickness of depletion region, V_{bi} and V are built-in voltage and diode voltage respectively. In addition, b_s is photon flux density and $x_{p,n}$, $w_{p,n}$ are total and depleted thickness of the p and n-regions respectively. Note that the equations are modified by multiplying with an additional term which is '$\left(1-\frac{{W_{dep}}^2}{\mu\tau(V_{bi}-V)}\right)$'. It is generally assumed to be equal to '1' since, the recombination in depletion region is neglected. However, recombination process for thick depletion regions should not be neglected. This term represent the carrier collection probability in the depletion region which could be less than '1'. The light generation current density in the space charge region is also given with the same coefficient by [43]:

$$J_{scr}\ =\left(1-\frac{{W_{dep}}^2}{\mu\tau(V_{bi}-V)}\right)q(1-R)b_se^{-\alpha(x_p-w_p)}. \tag{8}$$

Total short circuit current density is calculated by using the following relation [43].

$$J_{sc}\ =-j_n(-w_p)-j_p(-w_n)-j_{scr}\ . \tag{9}$$

Since pin diode is assumed to have a wider depletion thickness than a regular pn diode, the dark current density dominated by recombination process in the depletion region. Thus, the following equation is used to obtain dark current density in pin solar cells [43]:

$$J_o = \frac{\mathrm{q}n_i W_{dep}}{\tau} \frac{2\sinh(\mathrm{qV}/2kT)}{q(V_{bi}-V)/kT} . \quad (10)$$

From this, the diode output current can be calculated simply,

$$J = J_o - J_{sc} . \quad (11)$$

The open circuit voltage (V_{oc}) was determined numerically since; there is a lack of analytical relation between currents and the open circuit voltage. Finally, the resultant efficiency (η) of the solar cell is given by:

$$\eta = \frac{J_{sc}V_{oc}FF}{P_{in}} , \quad (12)$$

where FF is the fill factor and P_{in} is the total power of the incident light. Here, we also used P_{in} as the total power of the absorbed part of the spectrum to get a reference for a multi-junction solar cell operation since; ~2.3 eV wide band gap solar cell should be used as the top junction of a tandem cell and would transmit the sun light with energies less than ~2.3 eV.

2.3. Results and Discussion

Figure 2.3(a) and (b) shows the variation of total short circuit current density and the contribution of depletion region to it with respect to intrinsic layer thickness under

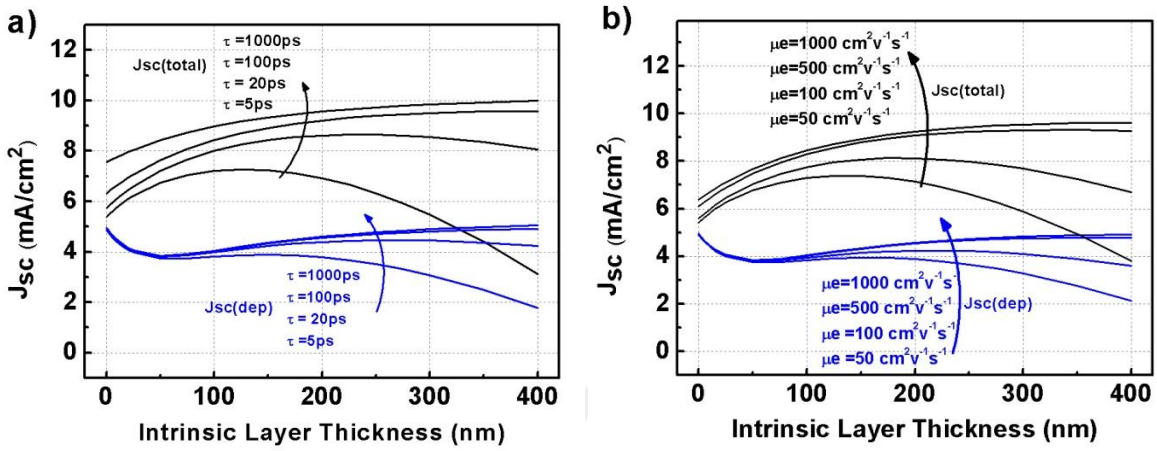

Figure 2.3. Short circuit current density and its amount generated in the depletion region variation as a function of intrinsiic layer thickness under varying carrier (a) lifetime and (b) mobility

varying minority carrier lifetime and electron mobility respectively. Firstly, it is clear that short circuit current density can be boosted by growing certain amount of intrinsic layer thickness for all over the range of the given parameters. Secondly, it is observed that in all cases; more than half of the total short circuit current density is generated from depletion regions which are formed by intrinsic layer especially when intrinsic layer thickness is greater than 70 nm. When it is shorter, the depletion region spreads into p-type region which lowers the hole diffusion current density generated in undepleted part of the p-type region. Thirdly, it is noteworthy that for high minority carrier lifetime (>100 ps) and electron mobility (>500 $cm^2V^{-1}s^{-1}$), short circuit current density increases continuously over the whole range of intrinsic layer thickness. However, it may suffer from the increase in the thickness of intrinsic layer when the minority carrier lifetime and electron mobility are below the values given above.

The explanation for the current drop is as follows. As the thickness of intrinsic region increases, the field across the depletion region decreases. This will shorten the drift length of the carriers (the product of minority carrier mobility, lifetime and electric field) which is taken into account in the first term of the equations (6), (7) and (8). If the depletion gets thicker or the product of minority carrier mobility and lifetime decreases, the short circuit current decreases accordingly which is reasonable since, the electric field becomes smaller and the diffusion length become too low for electrons and holes to be completely swept over a thick depletion region towards their terminals.

Current-voltage (I-V) characteristics of the pin solar cells are given as a function of T_{int} under varying electron minority carrier lifetime (τ_e) of 5, 20, 100 and 1000ps in the Figure 2.4(a), (b), (c) and (d) respectively. The short circuit current density analysis has been shown in Figure 2.3a and explained in details. The analysis of open circuit voltage (V_{oc}) is as follows. It is clearly seen that V_{oc} drops as T_{int} increases which is valid for all τ_e's. However, the amount of the drop strongly depends on τ_e. From Figure 2.4(d), it can be seen that V_{oc} slightly decreases from 2.16V (without intrinsic region) to 2.04V (with $T_{int}\ of\ 400nm$) under τ_e of 1ns. Whereas; it decreases sharply from 1.9V (without intrinsic region) to 0.8V (with $T_{int}\ of\ 400nm$) under τ_e of 5ps as shown in Figure 2.4(a). There are two possible mechanisms responsible for the V_{oc} drops. First reason can be explained from the equation (10) in which dark current is proportional to depletion region thickness and inversely proportional to average lifetime. Thus, V_{oc} drops as depletion thickness increases or average mobility decreases. But this drop is relatively small. The second and the dominant reason for sharp drop is the decrease in the electric field as

operating voltage increases also, the decrease in diffusion length under shorter τ_e which eventually results in an increase of carrier recombination.

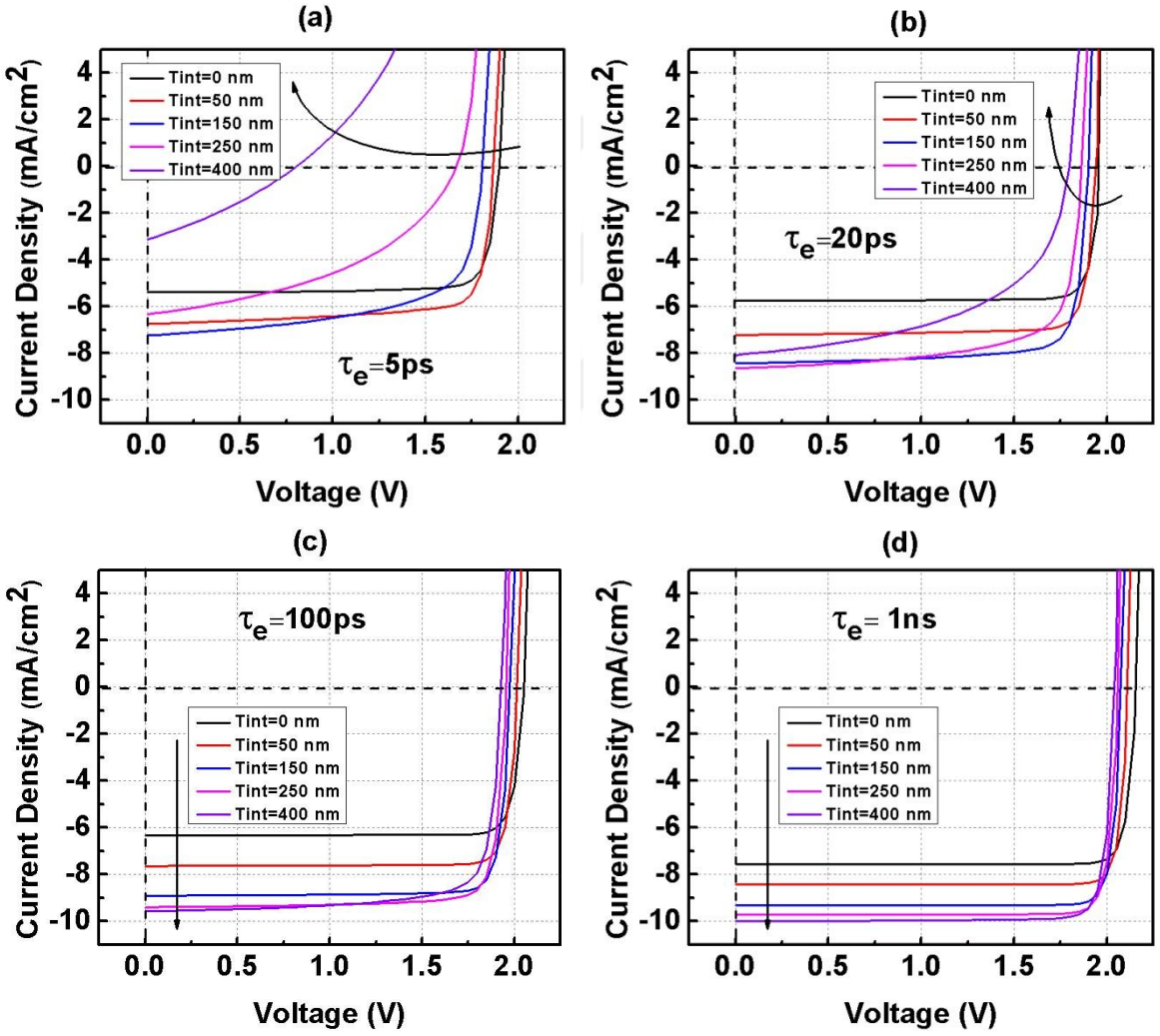

Figure 2.4. I-V plots of the solar cells with varying intrinsic region thickness under (a)τ_e=5 ps, (b)τ_e=20 ps,(c)τ_e=100 ps and (d)τ_e=1 ns (Intrinsic layer thickness increases in the direction of the arrows.)

Figure 2.5(a), (b), (c) and (d) shows the simulation of same structure with Figure 2.4 but, the varying parameter is electron mobility which is 50, 100, 500 and 1000 $cm^2V^{-1}s^{-1}$ respectively. From Figure 2.5(d), it can be seen that V_{oc} decreases slowly from 2.02V

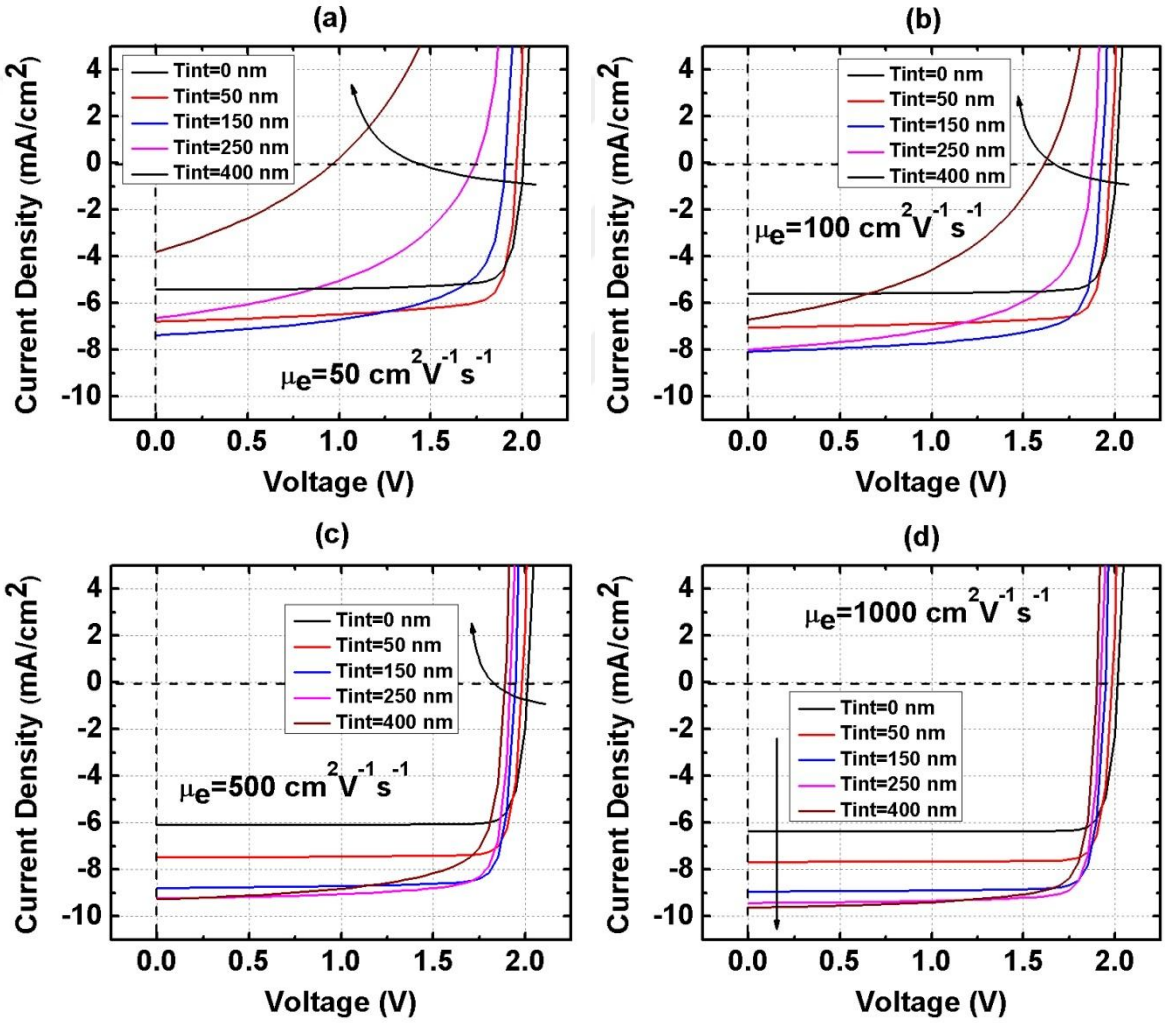

Figure 2.5. I-V plots of the solar cells with varying intrinsic region thickness under (a)μ_e =50$cm^2V^{-1}s^{-1}$, (b)μ_e =100$cm^2V^{-1}s^{-1}$,(c)μ_e =500$cm^2V^{-1}s^{-1}$ and (d)μ_e =1000$cm^2V^{-1}s^{-1}$ (Intrinsic layer thickness increases in the direction of the arrows.)

(without intrinsic region) to 1.91V (with $T_{int}\ of\ 400nm$) under μ_e of 1000 $cm^2V^{-1}s^{-1}$. On the other hand; it decreases sharply from 2.02V (without intrinsic region) to 0.95V (with $T_{int}\ of\ 400nm$) under μ_e of 50 $cm^2V^{-1}s^{-1}$ as shown in Figure 2.4(a). The results depicted in Figure 2.4 and 2.5 seem to show similar I-V behaviors since; both of the parameters (τ_e and μ_e) are proportional to the square of diffusion length which controls the characteristics. However, it is noteworthy that V_{oc}'s are independent from carrier mobility when T_{int} is relatively small (<50nm).

The fill factors (FF) as a function of intrinsic layer thickness (T_{int}) are depicted in Figure 2.6 (a) and (b) under varying carrier lifetime and mobility respectively. The maximum FF is ~0.9 according to our results which is higher than the maximum theoretical value of 0.83 [44]. Since the model used to obtain dark current (equation 10)

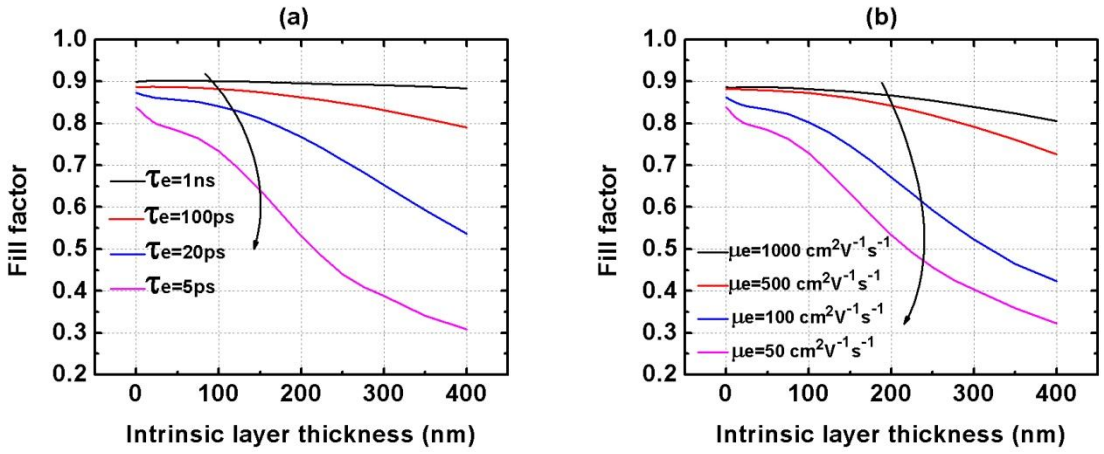

Figure 2.6. Variation of the Fill Factors with intrinsic carrier concentration under (a) carrier lifetime and (b) carrier mobility (Parameters decrease in the direction of arrows)

is based on recombination process in the depletion region for both carriers, the resultant FF values are slightly higher than the expected theoretical values of pn diode solar cell equations. It is obvious from both figures that FF decreases as T_{int} increases however; the fall of FF is much lower when τ_e>~100ps and/or μ_e>~500 $cm^2V^{-1}s^{-1}$. Since in these cases, the diffusion lengths are high enough for carriers to diffuse to their terminal before they recombine in the depletion region even under low field in the intrinsic region.

Figure 2.7 depicts the single and tandem cell efficiencies of the simulated 30% InGaN pin solar cells under varying intrinsic region thickness as a function of (a) minority carrier lifetime and (b) minority carrier mobility. Efficiency in tandem cell corresponds to the efficiency of the solar cell with respect to the absorbed part of the spectrum which is

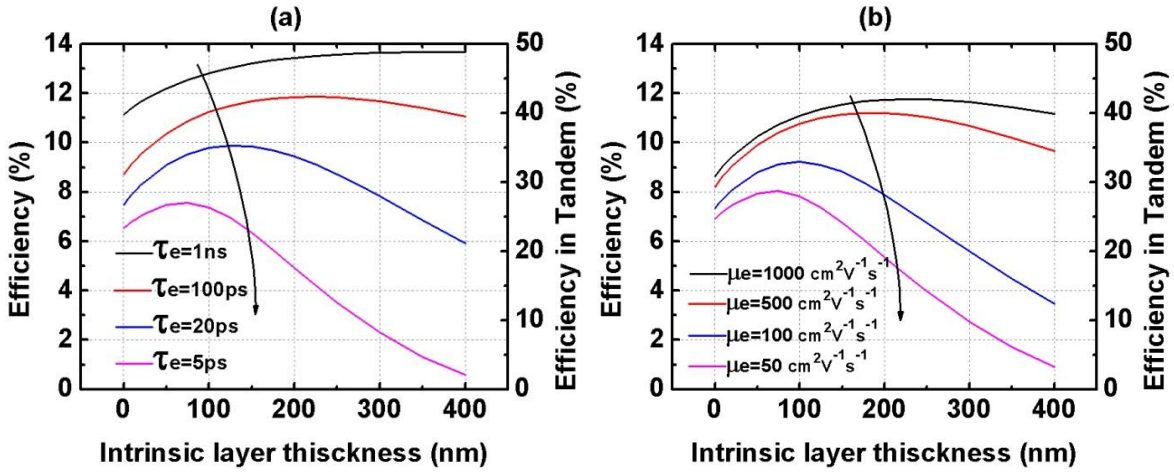

Figure 2.7. Single and tandem cell efficiency as a function of intrinsic layer thickness under varying (a)carrier lifetime and (b)carrier mobility

important since, the part of the solar spectrum with less than ~2.3 eV is not absorbed thus, in a tandem cell this energy is transferred to lower band gap junctions. It is

noteworthy that in all cases efficiency of the solar cells can be increased with some certain thickness of intrinsic region which is high for high carrier mobility and/or carrier lifetime. In addition, the thickness of the intrinsic region is critical since, having a thicker intrinsic region than the optimum thickness is detrimental for the solar cell operation and it can result in even less than the one for the cells formed without intrinsic region. In Figure 2.7 (a) and (b), although both efficiency variations seem similar, carrier lifetime variation results in relatively higher efficiency variation under default parameters ($\tau_e = 50ps\ and\ \mu_e \sim 444cm^2V^{-1}s^{-1}$) which is obvious especially when the thickness of the intrinsic region is relatively thin ($T_{int} < 50nm$). The maximum efficiency obtained under carrier life time variation with T_{int} of 400nm is around 14% for a single and 50% for a tandem cell. This is around 12% for a single cell and 42% for a tandem cell under carrier mobility variation with an T_{int} of 225nm. From the Figure 2.7, it is calculated that the pn junction solar cell efficiency can be increased by 36% if a pin design with appropriate intrinsic layer thickness is used. It should be kept in mind that these results are valid with the given structure of the solar cell and under the assumptions made.

2.4. Conclusions

The simulation of the 2.3 eV InGaN pin homojunction solar cell has been carried out under carrier mobility and lifetime variation to study the effects of intrinsic region thickness and material parameters on the solar cell operation. Although fill factors and open circuit voltages have been shown to decrease continuously by increasing the intrinsic layer thickness, short circuit current can be boosted so that the efficiency can be increased. It has been shown that having a certain thickness of intrinsic region can boost

the efficiency of the simulated pn junction solar cells by 36%. Moreover, the intrinsic layer thickness shown to be so critical especially when carrier mobility and lifetime is relatively low since, the efficiency can fall down dramatically if the intrinsic region is thicker than the optimal thickness of the particular cell which is a strong function of carrier lifetime and mobility.

However, it should be noted that there are couple of current technological limits towards the realization of the simulated 2.3 eV homojunction pin InGaN solar cells. Firstly, it has been shown that undoped GaN crystal shows n-type conduction ($<1x10^{16}$) because of Ga vacancies and native negative ions [45, 46]. Thus, obtaining an intrinsic region with very low carrier concentration is still under research. Secondly, due to the high lattice mismatch between GaN and InN, growing thicker than the critical thickness of InGaN results in relaxed layers which degrades the device operation. This effect is more pronounced as higher In mole fractions are introduced. Although there are problems with the realization of the simulated solar cells, the simulation results are expected to improve the understanding of the characteristics of 2.3 eV InGaN pin solar cell.

Chapter 3: N-Polar III- Nitride LEDs

In this chapter, N-polar LEDs are investigated both experimentally and theoretically for the first time to improve the understanding of reversed polarization field in nitride LEDs. In the first place Silvaco Atlas simulation results are shown to compare Ga- and N-polar structures. In the following part, world's first N-polar green LED is characterized experimentally.

3.1 Introduction

InGaN-based laser diodes (LD) and light emitting diodes (LED) emitting in the UV and blue wavelength range have found wide applications in optical storage and lighting applications [47,48]. There have been many studies on various planes of nitride crystals to obtain LEDs and LDs operating at longer wavelengths with high efficiencies [49,50]. More than 50% external quantum efficiencies (EQE) have been achieved for blue LEDs with both c-plane and semi-polar orientations whereas the maximum EQE ever reported for a green LED is 30% [50]. One of the main reasons for decreasing efficiency for longer wavelengths is that emitters for green and longer wavelengths still pose significant growth and device design challenges [51]. Firstly, due to the higher volatility of In species, higher In content InGaN requires lower growth temperatures than the optimal growth temperature of GaN. This mismatch in optimal growth temperatures leads to challenges in the growth of high quality InGaN/GaN multiple quantum well (MQW) emitters. Secondly, polarization effects are more pronounced as the In composition is

increased, It is expected that the relatively high polarization fields in c-plane oriented InGaN/GaN emitters could lead to poor carrier confinement and consequently poor efficiency in LED structures.

The N-polar orientation of GaN has several advantages that make it attractive for high In composition InGaN growth. N-polar InN can be grown by plasma-assisted molecular beam epitaxy PAMBE at higher temperatures (approximately 100^0C higher) than In-polar InN [52,53], This is attributed to the higher stability of InN on the N-polar surface. Recent work on N-polar InGaN growth demonstrated significantly higher growth temperatures and In incorporation on N-polar InGaN when compared to Ga-polar InGaN [54]. The direction of the spontaneous and piezoelectric polarization in N-polar is reversed from that of Ga-polar, which may provide advantages for LED operations. In addition, polarization plays a critical role in device operation of all polar emitters, and investigation of N-polar InGaN-based heterostructure devices provides a route to investigate these effects. Since the polarization field increases with In composition, these effects are more pronounced as longer emission wavelengths are targeted.

Although N-polar electronic devices with performance comparable to Ga-polar ones have been reported [55], there are relatively fewer reports on N-polar InGaN growth for optoelectronic applications [56,57,58], In this report, we report on the simulations, growth and optical characterization of N-polar InGaN based MQW LED grown by PAMBE.

3.2 Simulation of Ga- and N-Polar Single-Quantum-Well (SQW) LEDs

Silvaco Atlas simulations of SQW LEDs with $In_{0.18}Ga_{0.82}N$ (~2.82eV) have also been realized for extensive observation of device characteristics to compare both polarization directions. The SQW 2.82 eV LED structure is depicted in Figure 3.1. The models of k.p,

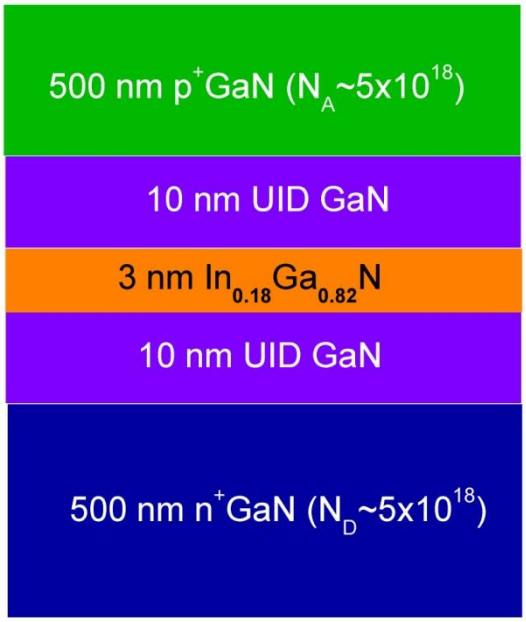

Figure 3.1. The epitaxial structure of the simulated LEDs.

chuang, incomplete, consrh, auger, optr and for the quantum well; lorentz spontaneous chuang are used in the simulation. Widely accepted values for the parameters are used for SCH recombination time, auger recombination coefficient and capture rate for radiative recombination. These parameters are; 1 ns, 1e-34 cm^6/s and 1.1e-8 cm^3/s respectively.

The electric field intensity variation across the devices is shown for various forward voltages (V_F) for Ga and N-polarity in Figure 3.2 (a) and (b). It is noted that the zero-bias

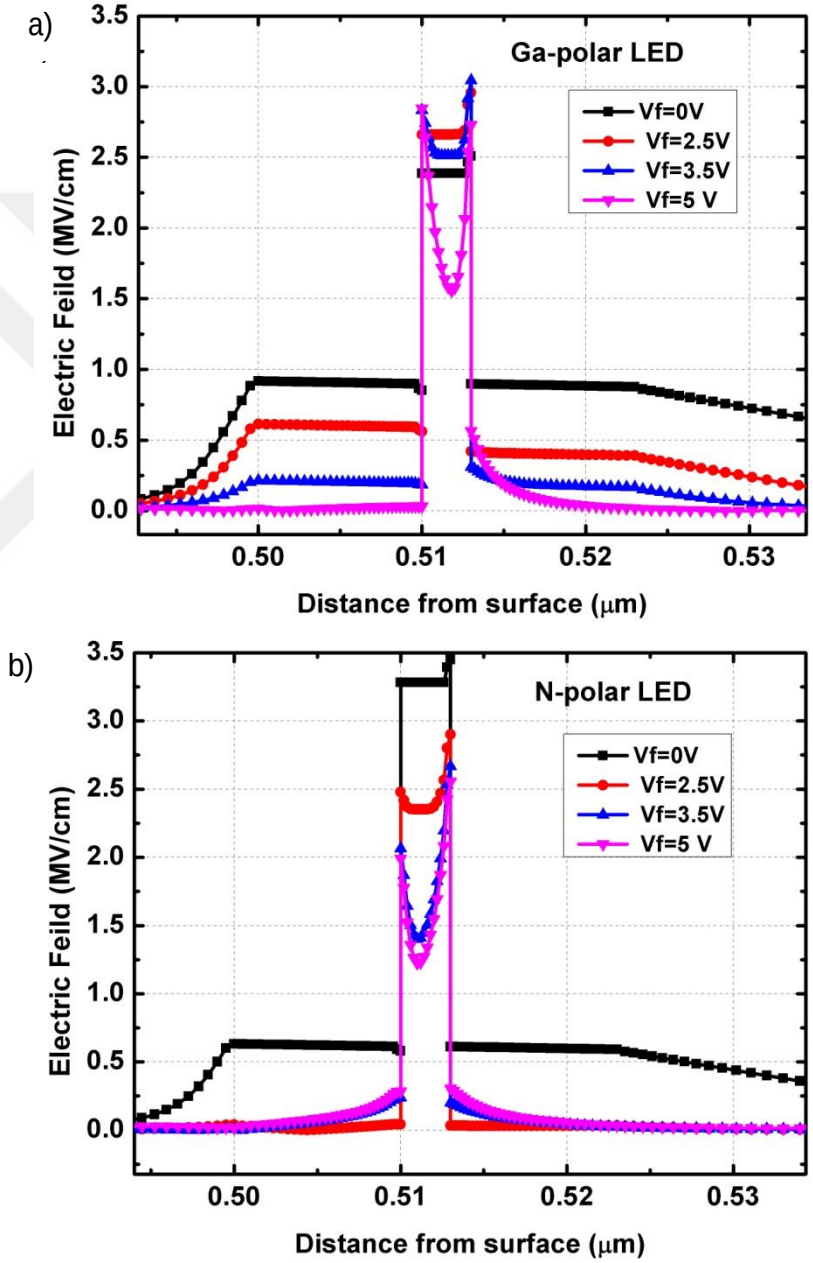

Figure 3.2. Electric field intensity profile for (a)Ga- and (b)N-polar LEDs at V_F=0, 2.5, 3.5, 5 V.

electric field in the QW of Ga-polar device is ~2.4 MV/cm whereas it is 3.3 MV/cm for N-polar. However, as the applied voltage increased to 2.5V the field in Ga-polar QW increases to ~2.7 MV/cm whereas it decreases to ~2.3 MV/cm for N-polar LED. The further increase in the applied bias leads to carrier injection into QWs and charge screening take place due to the coulomb force which results in damping of electric field. It is noted that the field intensity at the interface of the Ga-polar QW increases with an increase in applied bias on the other hand it decreases in N-polar QW. The reason of this behavior is that the bias induced electric field is in the same direction with Ga-polar internal polarization field whereas it is reversed for N-polar device. Thus, N-polar LED is expected to suffer less from QCSE.

The energy band diagrams of both LEDs at V_F=4 V are depicted in Figure 3.3(a) and (b). As it is seen from Figure 3.3(a), polarization charges in Ga-polar device generates a potential barrier for electron and hole injection which results in high turn on voltages. I-V characteristics of the device showed turn on voltage ~3.6 V (inset of Figure 3.3(a)). In the case of N-polar device, there is no potential barrier for carrier injection (Figure 3.3(b)) thus, device shows lower turn on voltage value ~ 2.75 V (inset of Figure 3.3(b)). Having ~1 V lower operating voltage leads to a considerable increase in wall-plug efficiency of nitride LEDs.

In addition to operation at lower voltages, N-polar LEDs are expected to show leakage current suppressing. As the band structures in Figure 3.3 are compared, it is seen that the conduction band energy level (E_C) and valance band energy level (E_V) across the QW region of Ga-polar LED are aligned in such a way that E_C close to n-GaN is higher than E_C close to p-GaN. Similarly, E_V close to p-GaN is lower than E_V close to n-GaN. These

band alignments should result in electron and hole leakage across the Ga-polar device. However, the polarization charges in N-polar device generates extra barrier for electrons

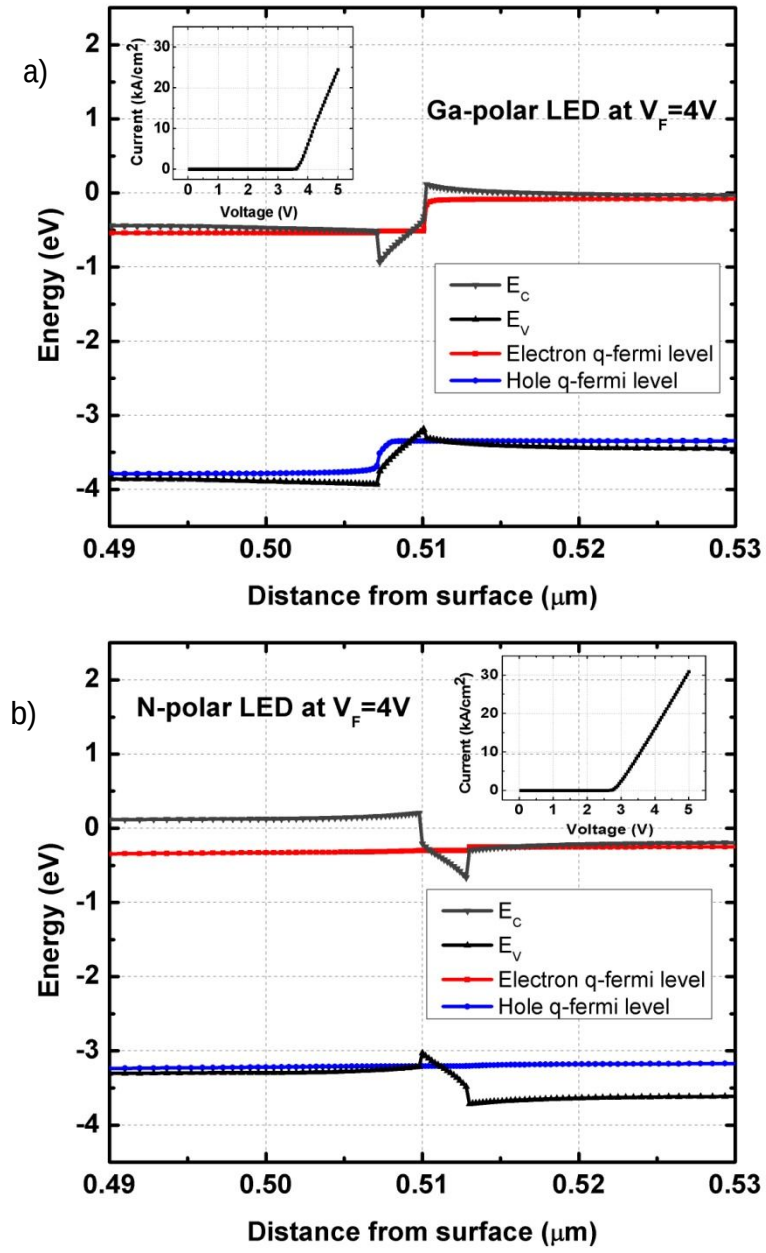

Figure 3.3. Energy band diagrams of (a) Ga and (b)N-polar SQW LEDs at 4 V forward bias. The insets show I-V characteristics of the devices.

and holes so that the leakage current would be suppressed. This analysis form the band diagrams is verified by the simulated current density values across the devices. The

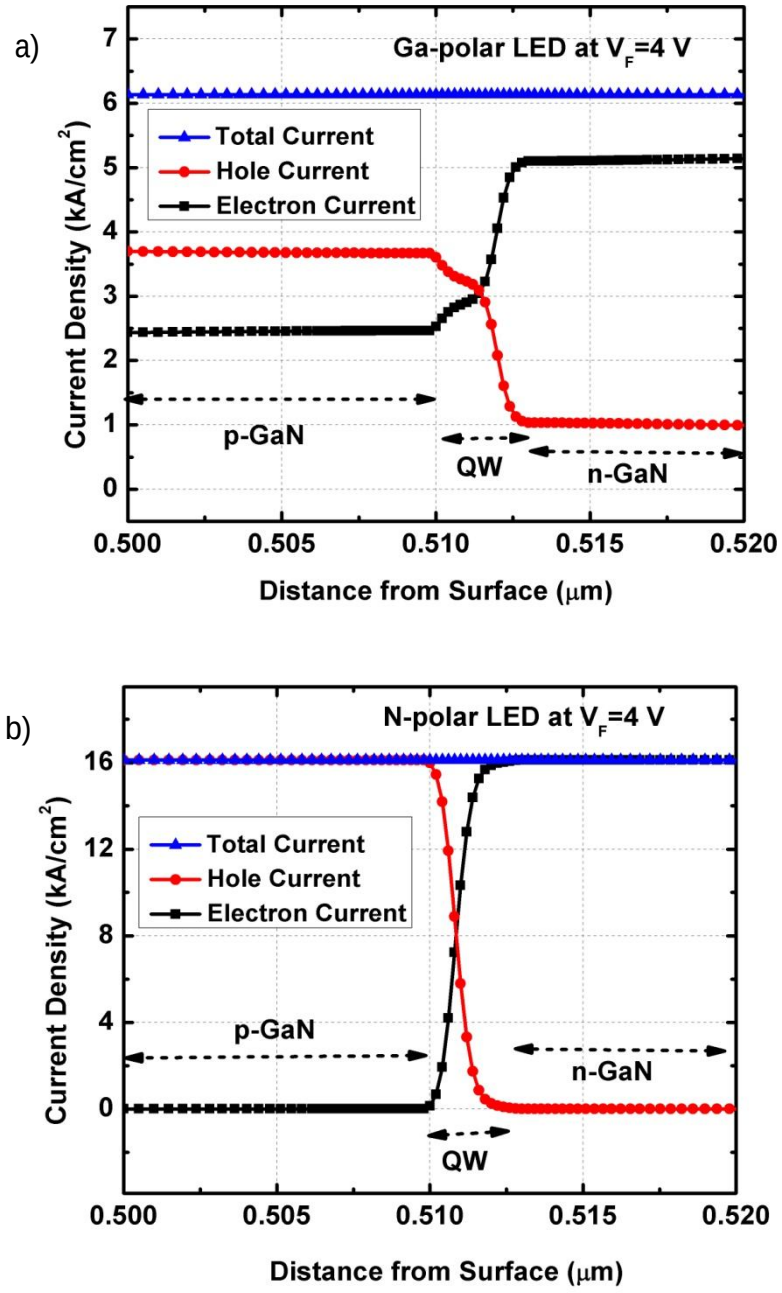

Figure 3.4. Current density profiles throughout the (a) Ga and (b) N-polar LED.

simulated current density values throughout the Ga and N-polar LEDs are given in Figure 3.4 (a) and (b) respectively. Ga-polar device showed both electron and hole overflow across the device where electron overflow in p-GaN is ~40% of the total current and hole overflow current is ~15% of the total current in n-GaN layer. The overflowing electrons and holes do not contribute to radiative emission and they eventually get lost in a recombination process with the majority carriers in the n and p-type regions. The results of N-polar LED shows no electron and hole leakage even though the current density values are considerably higher than the Ga-polar device. This kind of carrier overflow suppression mechanism in the absence of AlGaN electron blocking layer is expected to boost the efficiency characteristics of the nitride LEDs even at very high current density values. Such a property would be extremely beneficial for laser diode operations.

3.3 Experimental Research

3.3.1 Experimental Procedure

The sample used in this study was grown on N-polar free standing LED quality GaN template (dislocation density ~ 10^8 cm^{-2}) obtained from Lumilog by rf-plasma assisted molecular beam epitaxy in a Veeco Gen 930 system equipped with standard Knudsen cells for Ga and In [59]. Active nitrogen was supplied using a Veeco RF plasma source. Following the growth model for N-polar InGaN growth by PAMBE [54], a Ga-flux was chosen to achieve 29 % In mole fraction at a growth temperature of 600^0C. The growth of the active MQW region was performed in an N_2-limited and In rich growth regime with excess In coverage on the surface. The nominal growth rate defined by the N_2-stoichiometric flux in the absence of InGaN decomposition is 5 nm/min. However as

predicted by the growth model, for the In composition and growth temperature used for this growth, a reduced growth rate of 3.25 nm/min was calculated accounting for decomposition to grow 3 nm of $In_{0.29}Ga_{0.71}N$ quantum well and 12 nm $In_{0.14}Ga_{0.86}N$ barrier, the compositions being verified by X-ray diffraction (XRD) scan data with simulation (Figure 3.5(b)).

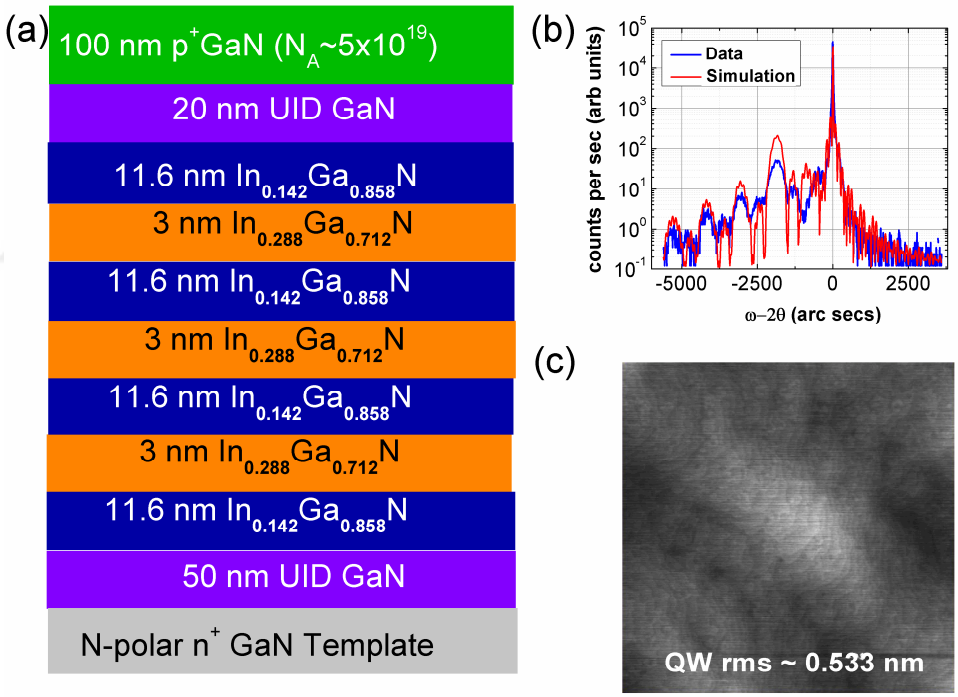

Figure 3.5. (a) The epitaxial design of the MQW green LED, (b) ω-2Θ XRD curves of the sample, and (c) AFM image of the sample showing the surface morphology of the quantum-well/barrier layer.

The growth of InGaN QW and a GaN (or InGaN) barrier without growth interruption with a single Ga effusion cell in PAMBE poses severe challenges because the growth temperature as well as the Ga flux required for the growth of QW and barrier is significantly different. An N_2-pulsing scheme was hence employed to grow the barrier where In and Ga shutters were kept open throughout with the Ga-flux at the same value as used for preceding quantum well layer growth. The duty cycle of the pulse was adjusted to get InGaN with a higher Ga mole fraction. To investigate the surface morphology of the QW layer, a test sample was grown in identical conditions with the growth intentionally terminated with a ~ 2 nm $In_{0.05}Ga_{0.95}N$ (to prevent decomposition) on a single 3 nm $In_{0.29}Ga_{0.71}N$ QW layer. The atomic force microscopy (AFM) image shows smooth surface morphology (Figure 3.5(c), 2 x 2 μm^2 scan).

LEDs were fabricated using conventional optical lithography. Ni / Au / Ni (5 / 5 / 1 nm) metal stack was evaporated to form the p-type electrode. Following the p contact evaporation, mesa isolation of the devices was performed by Cl–based inductively coupled plasma (ICP) etching with Cl_2 / BCl_3 / Ar (50 / 5 / 5 sccm) plasma under 40 W ICP power and 3 W RF power for 30 min. Finally, Ti / Au (20 / 100 nm) n-contact was deposited on the etched n-GaN layer. All measurements reported were performed on a 17,000 μm^2 device at room temperature under continuous wave operation..

3.3.2 Results and Discussion

Current-Voltage (I-V) characteristics of a typical N-polar LED are shown in the inset of Figure 3.6. The differential resistance and turn-on voltage were 0.012 $\Omega.cm^2$ (72 Ω) and

5V, respectively. The image of the forward biased LED is shown in the inset of Figure 3.6. We attribute the light intensity variation observed across the contact and the presence of high turn-on voltage to unoptimized ohmic contacts and growth of p-GaN layer. The electroluminescence (EL) spectra for increasing driving current are shown in Fig. 3.6. The maximum current driven in this regime was 30 mA, corresponding to a density of 176 A/cm^2. The peak wavelengths, peak intensities and full width at half maximum (FWHM) as a function of driving current are shown in Fig. 3.7. An increase in the driven

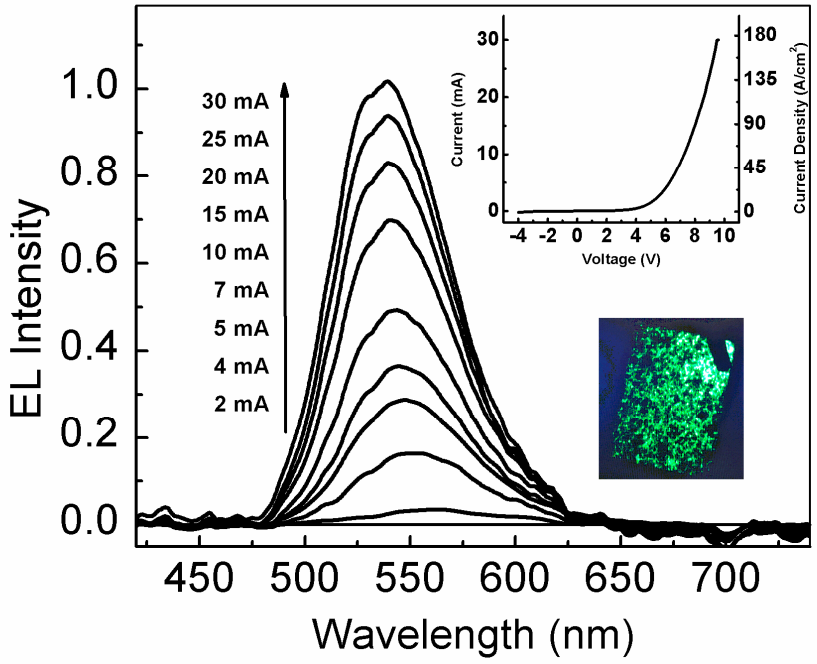

Figure 3.6. EL spectra as a function of DC driving currents varying from 2 to 30-mA (11 to 176 A / cm^2). The above inset shows the I-V characteristics of the 17,000 μm^2 LED and the bottom one shows the image of the forward biased LED.

current results in a linear increase in the EL emission intensity up to 88 A/cm^2, and after that point, it starts to saturate depending on the increasing heating effect on the device operation. The peak wavelengths were measured as 563 and 540 nm at 2 and 30 mA, respectively. The 23 nm blue shift over 28 mA (165A /cm^2) is attributed to screening of the piezoelectric field by electrons and holes at higher injection current density [60]. Note that there is only 0.7 nm blue shift from 88 to 176 A/cm^2 which may result from a competition between state-filling effect and heat generation [61]. The FWHM variation

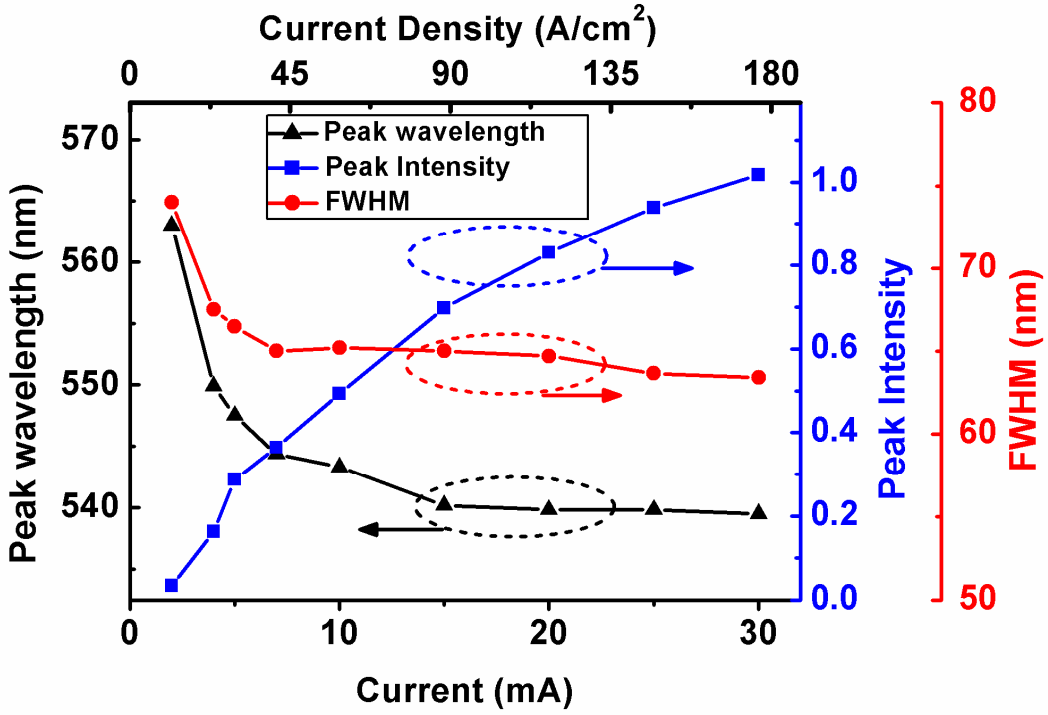

Figure 3.7. EL emission peak intensities (normalized to the highest value), peak wavelengths and FWHMs as a function of driving current from 2 mA to 30 mA (11 to 176 A / cm^2).

as a function of driven current showed a fast decreasing trend from 74 to 65 nm up to a current density of 45 A/cm^2 then, it slowly decreases to a value ~63.4 nm for the rest of the current density regime. Based on the previous Ga-polar LED reports, it can be observed that FWHM decreases as current increases at low current density regimes (<~25 A/cm^2) and increases at higher current densities [61].

We note that the measured FWHM is higher than that observed in the state-of-art green LEDs grown, for example, by metal organic chemical vapor deposition (MOCVD) [61, 62]. The growth conditions used for the LEDs described in this work were optimized only to achieve the required emission wavelength. The FWHM is mostly dependent on the micro scale compositional and thickness uniformity of the InGaN wells, which in turn are greatly dependent on the growth parameters such as temperature, flux etc. We have not carried out growth optimization to minimize the FWHM, and it is likely that the fluctuations in Indium and quantum well thickness contribute to the FWHM. Further investigation in this direction should lead to lower FWHM, and better emission results.

The decrease of FWHM at low current density has been attributed to band filling effects caused by potential fluctuations, while the increase at higher current density is due to screening charges and excess heat generation [60, 63, 64]. The behavior of N-polar LED in the present study might be attributed to the dominating effect of In fluctuations due to the unoptimized growth conditions which also results in greater than expected FWHM values for this wavelength range. While further investigations are needed to clarify these issues, the FWHM saturation at high current regimes might result from a competition

between band filling effect and excess heat generation which can be seen as a deviation from linearity of the peak intensity variation with current density (Figure 3.7).

3.4 Conclusions

The characteristics of Ga- and N-polar blue (2.82eV) InGaN SQW LEDs have been simulated. The simulation results showed that N-polar LED suffer less from QCSE and have ~1V lower turn-on voltage compared to Ga-polar LED. More importantly, N-polar LED does not show any electron or hole overflow even at very high current densities which is expected to enhance high current operations of nitride LEDs. In the experimental part, first MBE grown N-face InGaN green LED was realized and fabricated successfully. The EL measurement results of the device showed a short blue shift from 563 to 540 nm and a decreasing FWHM from 74 to 63.4 nm under 165 A/cm^2 current range. Our results show that the EL FWHM values are high and saturate at high current range. We speculate that this behavior may result from un-optimized growth conditions which cause higher In fluctuations. It is noted that our LED shows efficiency droop at high current density values we attribute this characteristics to already discussed issues of the LED growth. Both of the simulation and experimental demonstrations of N-polar InGaN-based LEDs could lead to improved understanding of polarization effects on LED performance.

References

1) J. I. Pankove, E. A. Miller, J. E. Berkeyheiser, *RCA Review* 32, 383 (1971).

2) H. P. Maruska, W.C. Rhines, D.A. Stevenson, *Mat. Res. Bull.* 7 777 (1972).

3) H. P. Maruska, L. J. Anderson, D. A. Stevenson, *J. Electrochem. Soc.*, 121, 1202 (1974)

4) I. Akasaki, and I. Hayashi, *Kogyo Gijutsu* **17**, 48 (1976) [In Japanese].

5) H. Amano, N. Sawaki, I. Akasaki, and Y. Toyoda, *Appl. Phys. Lett.* **48**, 353 (1986).

6) S. Nakamura and T. Mukai, Jpn. J. of Appl. Phys. 31, p. L1457(1992).

7) H. Amano, M. Kito, K. Hiramatsu, and I Akasaki, *Jpn. J. Appl. Phys.* **28** L2112 (1989).

8) S. Nakamura, T. Mukai, M. Senoh, and N. Iwasa, *Jpn. J. Appl. Phys.* 31, L139

(1992).

9) S. Nakamura, M. Senoh, and T. Mukai, *Jpn. J. Appl. Phys.* **32**, L8 (1993).

10) S. Nakamura, N. Senoh, N. Iwasa, S. Nagahama, *Jpn. J. Appl. Phys.* **34**, L797 (1995).

11) J. Neugebauer, phys. stat. sol. (b) 227, 93 (2001).

12) A. R. Smith, R. M. Feenstra, D. W. Greve, M.-S. Shin, M. Skowronski,

J. Neugebauer and J. E. Northrup, Surf. Sci. 423, 70 (1999).

13) H. Masui, S. Keller, N. Fellows, N. A. Fichtenbaum, M. Furukawa, S. Nakamura, U. K. Mishra, and S. P. DenBaars: Jpn. J. Appl. Phys. **48** (2009) 071003

14) S. Nakamura and G. Fasol, The Blue Laser Diode (Springer Verlag, 1997).

15) F. Bernardini, V. Fiorentini and D. Vanderbilt, Phys. Rev. B 56, R10024 (1997).

16) F. Bernardini and V. Fiorentini, *Phys. Stat. Sol. (b)* **216**, 391, 1999.

17) Sami Suihkonen: PhD dissertation (2008).

18) G. Sun, Y. J. Ding, G. Liu, G.S. Huang, H.Zhao, N. Tansu and J. B. Khurgin Appl. Phys. Lett. **97**, 021904 (2010).

19) International Energy Agency: http://www.iea.org

20) Francois Cellier, The Oil Drum (2008): europe.theoildrum.com/node/4002

21) Spire Semiconductor: Optics.org Oct 2010.

22) K. Kumakura, T. Makimoto, T. Hashizume, T. Fukui and H. Hasegawa, J. Crys. Growth 298 (2007) 787.

23) R. R. King, R. A. Sherif, C. M. Fetzer, and P. C. Colter, "Advances in High-Efficiency Multijunction Terrestrial Concentrator Cells and Receivers," in Proc. Of NCPV and Solar Program Review Meeting 2003, 2003, pp. 211

24) Z. Q. Li, M. Lestradet, Y. G. Xiao and S. Li, Phy. Status Solidi A, 1 (2010).

25) Wu J, Walukiewicz W, Yu K M, Ager J W III, Haller E E, Lu H, Schaff W J, Saito Y and Nanishi Y Appl. Phys. Lett. **80** 3967 (2002).

26) Xiao H L, Wang X L, Wang J X, Zhang N H, Liu H X, Zeng Y P, Li J M and Wang Z G 2005 J. Cryst. Growth **276** 401.

27) K. Tadatomo, H. Okagawa, Y. Ohuchi, T. Tsunekawa, Y. Imada, M. Kato and T. Taguchi Jpn. J. Appl. Phy. **40** (2001) L 583-L 585.

28) Y. Zhao, J. Sonoda, C. Pan, S. Brinkley, I. Koslow, K.Fujito, H. Ohta, S. P. DenBaars and S. Nakamura. Appl. Phys. Express **3** (2010) 102101.

29) P. Stauss, A. Walter, J. Baur, and B. Hahn: presented at 7th Int. Conf. Nitride Semiconductors (ICNS7) (2007).

30) C. Yang, X. Wang, H. Xiao, J. Ran, C. Wang, G. Hu, X. Wang, X. Zhang, J. Li and J. Li Phy. Stat. Sol. (a) **204** No. 12, 4288-4291 (2007).

31) H. Hamzaoui, A. S. Bouazzi and B. Rezig 2005 Sol. Energy Mater. Sol. Cells **87** 595

32) O. Jani, I. Ferguson, C. Honsberg and S. Kurtz Appl. Phy. Lett. **91** 132117 (2007).

33) W. Walukiewicz, J. W. Ager, K. M. Yu, Z. Liliental-Weber, J. Wu, S. X. Li, R. E. Jones, and J. D. Denlinger, J. Phys. D 39, R83 (2006).

34) J. Wu, W. Walukiewicz, K. M. Yu, W. Shan, J. W. Ager, E. E.Haller, H. Lu, W. J. Schaff, W. K. Metzger, and S. Kurtz, J. Appl. Phys. 94, 6477 (2003).

35) K. Kumakura, T. Makimoto, N. Kobayashi, T. Hashizume, T. Fukui and H. Hasegawa Appl. Phys. Lett. **86** 052105 (2005)

36) K. Kumakura, T. Makimoto, N. Kobayashi, T. Hashizume, T. Fukui and H. Hasegawa J. Cryst. Growth **298** 787-790 (2007)

37) T.T. Mnatsakanov, M.E. Levinshtein, L.I. Pmortseva, S.N. Yurkov, G.S. Simin, M.A. Khan Solid-State Electron. **47** (2003) 111–115.

38) L. Hsu, R.E. Jones, S.X. Li, K.M. Yu, W. Walukiewicz J. Appl. Phys. **102** (2007) 073705-1–6.

39) http://www.ioffe.ru/SVA/NSM/Semicond/

40) J. Wu and W. Walukiewicz Superlattices and Microstructures, **34** 63-75 (2003).

41) R. Aleksiejunas, M. Sudzius, V. Gudelis, T. Malinauskas, K. Jarasiunas, Q. Fareed, R. Gaska, M.S. Shur, J. Yang, E. Kuokstis and M.A. Khan Phys. Ptat. Sol. (c) **0**, No. 7, 2686–2690 (2003).

42) G.F. Brown, J.W. Ager, W. Walukiewicz and J. Wu Solar Energy Materials & Solar Cells **94** (2010) 478-483

43) Jenny Nelson 'Physics of Solar Cells' p.132,222,223

44) R.A. Messenger, J. Ventre 'Photovoltaic system engineering' p.51

45) K. Saarinen, J. Nissila, J. Oila, V. Ranki, M. Hakala, M. J. Puska, P. Hautojarvi, J. Likonen, T. Suski, I. Grzegory, B. Lucznik and S. Porowski Physica B **273** (1999) 33-38

46) Cree: www.cree.com

47) S. Nakamura, M. Senoh, S. Nagahama, N. Iwasa, T. Yamada, T. Matsushita, H. Kiyoku, and Y. Sugimoto: Jpn. J. Appl. Phys. **35** (1996) L74.

48) S. Nakamura, M. Senon, and T. Mukai: Jpn. J. Appl. Phys. **32** (1993) L8.

49)T. Detchprohm, M. Zhu, Y. Li, L. Zhao, S. You, C. Wetzel, E. A. Preble, T. Paskova, and D. Hanser: Appl. Phys. Lett. **96** (2010) 051101.

50) Y. Zhao, J. Sonoda, C. Pan, S. Brinkley, I. Koslow, K.Fujito, H. Ohta, S. P. DenBaars, and S. Nakamura: Appl. Phys. Express **3** (2010) 102101

51) R. Stevenson: IEEE Spectrum **47** 3 (March 2010) 34.

52) K. Xu and A. Yoshikawa: Appl. Phys. Lett. **83** (2003) 251.

53) H. Naoi, F. Matsuda, T. Araki, A. Suzuki and Y. Nanishi: J. Cryst. Growth **269** (2004) 155.

54) D Nath, E. Gur, S. Ringel and Siddharth Rajan: Appl. Phys. Lett. **97** (2010) 071903

55) S. Rajan, A. Chini, M.H. Wong, J.S. Speck and U.K. Mishra: J. Appl. Phys.**102** (2007) 044501.

56) Joshua Abell: Dr. Thesis, Collage of Engineering, Boston University, Massachusetts (2008).

57) X.Q. Shen, T. Ide, M. Shimizu and H. Okumura: J. Cryst. Growth **237-239** (2002) 1148.

58) H. Masui, S. Keller, N. Fellows, N. A. Fichtenbaum, M. Furukawa, S. Nakamura, U. K. Mishra, and S. P. DenBaars: Jpn. J. Appl. Phys. **48** (2009) 071003.

59) Lumilog: www.lumilog.com

60) P. Perlin, C. Kisielowski, V. Iota, B. A. Weinstein, L. Mattos, N. A. Shaprio, J. Kruger, E. R. Weber, and J. Yang: Appl. Phys. Lett. **73** (1998) 2778.

61) M. Funato, M. Ueda, Y. Kawakami, Y. Narukawa, T. Kosugi, M. Takahashi and T. Mukai: Jpn. J. Appl. Phys. **45** 659 (2006).

62)Y. Lin, A. Chakraborty, S. Brinkley, H.C. Kuo, T. Melo, K. Fujito, J. S. Speck, S. P. DenBaars, and S. Nakamura: Appl. Phys. Lett. **94** (2009) 261108

63) Y. D. Qi, H. Liang, D. Wang, Z. D. Lu, W. Tang, and K. M. Lau: Appl. Phys. Lett. **86** (2005) 101903.

64) S. Yamamoto, Y. Zhao, C. Pan, R. B. Chung, K. Fujito, J. Sonoda, S. P. DenBaars, and S. Nakamura: Appl. Phys. Express **3** (2010) 122102.